Probing the Influence of Boron Nitride Doping on the Two-Dimensional qHP C_{60} Monolayer: An Investigation Integrating First-Principles and Classical Approaches

Sushma Yadav[a], Suchetana Sadhukhan[b], and Vivek K. Yadav[c,†,∗]

(a) Department of Chemical Engineering, IIT BHU, Varanasi, Uttar Pradesh 221011, India

(b) School of Advanced Sciences and Languages (SASL), VIT Bhopal University, Sehore, Madhya Pradesh 466114, India

(c) Department of Chemistry, University of Allahabad, Prayagraj, Uttar Pradesh 221001, India

This research investigates the electronic and dynamic properties of 2D qHP polymer sheets made of fullerene, with and without boron and nitrogen doping. Using density functional theory (DFT) with PBE and HSE functionals, including van der Waals interactions and classical simulations, we found that BN-doped qHP C60 materials exhibit enhanced conductivity and adsorption characteristics, demonstrating semiconducting behaviour with higher carrier mobility. qHP $C_{58}B_1N_1$ shows ultra-high conductivity ($\sim 10^{12}\ \Omega^{-1}cm^{-1}s^{-1}$ at room temperature). These qHP sheets have cohesive energies of -8.75 (C_{60}), -8.70 ($C_{58}B_1N_1$), and -8.67 ($C_{54}B_3N_3$), in the unit of eV, indicating greater stability than graphene and h-BN. Optical analysis suggests qHP C60 can absorb UV photons up to 1.1 eV, with a refractive index greater than one and an estimated optical bandgap of 0.95–1.65 eV. They have moderate direct electronic bandgaps and anisotropic mechanical properties, with Young's modulus of 180-200 GPa. These structures transition abruptly from elastic to fracture at a critical strain threshold, with similar thermal stability and melting points around 3900K.

1 Introduction

The allure of metal-free semiconductors with narrow bandgaps has captured significant attention in recent decades, proving exceptionally versatile for various electronic applications such as infrared devices, light-emitting diodes, electrocatalysts, and thermo-photovoltaics. This interest has been further fueled by the emergence of two-dimensional nanomaterials in material science and engineering following the groundbreaking discovery of graphene by a collaborative effort in the past decade [1–4].

Recently, a breakthrough occurred with the experimental realization of a single-crystal 2D carbon material, termed monolayer quasi-hexagonal-phase fullerene (C_{60}), boasting a semiconducting bandgap of approximately 1.6 eV [5]. This achievement addresses the issue of null bandgaps observed in other 2D carbon-based materials. Using an organic cation slicing strategy, researchers exfoliated quasi-hexagonal bulk single crystals to obtain monolayer polymeric C_{60}. Using an interlayer bonding cleavage strategy, they obtained large-sized C_{60} 2D crystals. These crystals exhibit a unique structure where C_{60} polymers form covalently bonded cluster cages within a plane. This clustering mechanism led to the formation of two stable crystals, namely closely packed quasi-hexagonal (qHP C_{60}) and quasi-tetragonal (qTP C_{60}) phases [5].

Monolayer C_{60} distinguishes itself from other 2D materials due to its larger surface area and increased active sites resulting from the quasi-0D network structures of C_{60} cages. It exhibits excellent thermodynamic stability and high carrier mobility, making it a promising candidate for photocatalytic water splitting [6–10]. Obtaining monolayer polymeric C60 involved an organic cation slicing strategy, yielding substantial-sized C_{60} 2D crystals with remarkable crystallinity and thermodynamic stability. Further exploration in these areas holds significant potential to unlock their full capabilities. Notably, Gao and colleagues' first-principles findings suggest that N-C_{60} fullerene could serve as a promising cathode catalyst for hydrogen fuel cells by facilitating the water formation reaction without encountering activation energy barriers [11]. Despite valuable insights from previous research, a comprehensive understanding of their electronic, optical, and mechanical characteristics is still awaited.

Peng and his team recently discovered that using a weakly screened hybrid functional in conjunction with time-dependent Hartree-Fock calculations can accurately reproduce the experimentally measured optical band gap of the monolayer of C_{60} [12,13]. The various phases of monolayer fullerene networks feature suitable band gaps, displaying high carrier mobility and appropriate band edges. These characteristics render them thermodynamically favourable for driving overall water splitting [14].

The deliberate choice of foreign elements in carbon-based 2D materials, ensuring an optimal carbon-to-doping element ratio, is crucial for customizing the electronic properties of these newly developed 2D materials. This process enhances their suitability for advanced device applications [15–20]. Various methods have emerged to refine nanomaterials' properties, such as surface defects, metal decoration, and transition metal doping. These approaches are extensively investigated through both experimental studies and DFT-based calculations. This understanding presents intriguing opportunities for customizing nanomaterials to fulfil the specific needs across various scientific and engineering domains [21–24].

Along with the first-principles DFT, the larger system size using force-field-based molecular dynamics (MD) simulations can pave the way for the thermodynamic stability and fracture patterns of qHPC_{60} and qTPC_{60}. Nevertheless, the doping effect on structural

† *Equal first author contribution*

∗*Corresponding author Email: vkyadav@allduniv.ac.in*

https://doi.org/10.26434/chemrxiv-2024-mzs2z **ORCID:** https://orcid.org/0000-0002-9142-4567 Content not peer-reviewed by ChemRxiv.

integrity with thermodynamic stability can impact their performance in their application as a new generation of carbon functional nanomaterials. In this regard, the mechanical and thermal stability of qHPC_{60}, qHP $C_{58}B_1N_1$ and qHP $C_{54}B_3N_3$ were systematically investigated in the scope of fully-atomistic force-field-based molecular dynamics simulations. A heating ramp protocol simulations were performed to obtain the melting point, and the mechanical behaviour was studied using the stress-strain relationship. The calculated Young Modulus agree with the experimental and theoretical findings. This article primarily focuses on a comprehensive analysis of the properties of qHPC_{60} (System-I) and qHP $C_{58}B_1N_1$ (with the highest mobility) (System-II), and qHP $C_{54}B_3N_3$ (System III) polymeric sheets, demonstrating unique characteristics. We present the calculation methodology, detailing the DFT methods and classical simulations. The Results and Discussion section explores the doped materials' structural and lattice dynamic stability. We examine the electronic band structure and projected density of the nanosheets' states, analyzing their mechanical and optical properties and comparing them with polymeric fullerene. Finally, we provide a concise summary of the significant findings obtained in this study.

2 Methodology

Using the Density Functional Theory (DFT) framework, first-principle simulations offer valuable quantum insights into nanostructured materials with high precision and cost-effectiveness. We conducted DFT calculations in this study using the QUANTUM ESPRESSO software package [25]. The Perdew-Burke-Ernzerhof (PBE) [26] functional described the electron-ion interaction using the generalized gradient approximation (GGA) [27]. A plane wave basis set with a kinetic energy cut-off of 50 Ry for electron density and 500 Ry for charge density was utilized to optimize the structural configuration of fullerene-based systems. Brillouin zone (BZ) integration was performed using a $8 \times 8 \times 1$ k-point grid for geometry optimization and $10 \times 10 \times 1$ for electronic structure calculations [28]. Atomic positions and cell parameters were fully relaxed until 10^{-8} eV energy convergence was achieved. Van der Waals interactions were accounted for using DFT-D3 dispersion corrections [29]. The HSE functional [30] was also employed to compute bandgaps with $5 \times 5 \times 1$ k-points due to the PBE functional's tendency to underestimate them. Electrical conductivity was calculated using the semi-classical Boltzmann equation under constant relaxation approximation, employing a dense $20 \times 20 \times 1$ k-mesh for transport property calculations. The unit cell was designed to include pure and one and three pairs of BN atoms doped per C_{60} fullerene, with a 20Å vacuum region introduced perpendicular to the sheet to prevent unwanted interactions between periodic images.

To examine the thermal and mechanical stability, the fully atomistic classical molecular dynamics simulations were performed using the tersoff potential as implemented in LAMMPS [31]. The fullerene structures have dimensions of 80.1*73.4 Å^2 with periodic boundary conditions and are composed of 4800 atoms. The length of the simulation box along the z-direction is 130 Å. The equations of motion are integrated using the velocity-Verlet algorithm, with a time-step of 0.5 fs. Before heating and stretching, the structures were equilibrated using an NPT ensemble at a constant temperature of 300 K using a Nose-Hoover thermostat for 200 ps. The structures were continuously stretched up to their complete structural failure (fracture) by applying a maximum strain of 25%. The tensile stretching simulations were performed here by only deforming in the y directions. Their thermal stability was investigated by heating up the structures from 300 K to 10,000 K by linearly increasing the temperature during 1 ns in an NVT ensemble. The molecular dynamics snapshots and trajectories were visualized using the visualization software VMD [32].

3 Results and discussion

3.1 Structural properties

Figure 1(a,b,c) depicts the fully relaxed structures of qHP's of C_{60}, $C_{58}B_1N_1$, and $C_{54}B_3N_3$. During optimization, atomic positions and cell parameters were relaxed using the vc-relax module of QE. The calculated lattice parameters "a" and "b" for (a) qHP C_{60}, and (b) qHP $C_{58}B_1N_1$, and c) qHP $C_{54}B_3N_3$ along the x-axis (y-axis) were determined to be 15.87 Å (9.14 Å), 15.87 Å (9.14 Å), and 15.84 Å (9.14 Å), respectively. With a B-N pair mimicking a C-C bond regarding electron count, the overall cell volume remains consistent with C_{60} following B-N doping.

The thermodynamic and structural stability of the three proposed nanosheets were evaluated by computing their formation and cohesive energies. The formation energy (E_{for}) is determined using Equation 1, while the cohesive energy (E_{coh}) can be calculated using Equation 2.

$$E_{for} = [E_{system} - (n_{CC}\mu_{CC} + n_{BN}\mu_{BN}]/n \quad (1)$$

whereas their cohesive energy (E_{coh}) can be calculated by using equation 2

$$E_{coh} = [E_{tot} - \sum_i n_i E_i]/n \quad (i = \text{C, B, N}) \quad (2)$$

In equation 1,n_{CC} and n_{BN} represent the CC and BN pairs in the proposed sheets, respectively, with the total number of C-C bonds in pristine qHP fullerene unit cell is assumed to be 180. The symbols μ_{CC} and μ_{BN} denote the chemical potential of C–C and B–N, respectively. The chemical potentials μ_{CC} and μ_{BN} obtained from graphene and BN sheets were -310.15 and -358.35 eV, respectively. The E_{for} for qHP's of C_{60}, $C_{58}B_1N_1$, and $C_{54}B_3N_3$ are found to be 201.95, 202.09, and 202.33, in units of eV, respectively. In the equation 2, E_{tot} denotes the total energy of three individual sheets, E_i represents the gas phase atomic energies of Carbon, Boron, and Nitrogen, and n represents the total number of atoms in the sheet. The calculated cohesive energies of C_{60}, $C_{58}B_1N_1$, and $C_{54}B_3N_3$ were found to be -8.76, -8.70 and -8.67, in units of eV, respectively. This shows that stability decreases monotonically with increasing B-N dopant concentration. A molecular structure with a more negative cohesive energy value indicates greater structural stability [33,34]. Our observations show that pristine C_{60} exhibits a notably higher negative cohesion energy value, whereas doped nanosheets showcase pre-

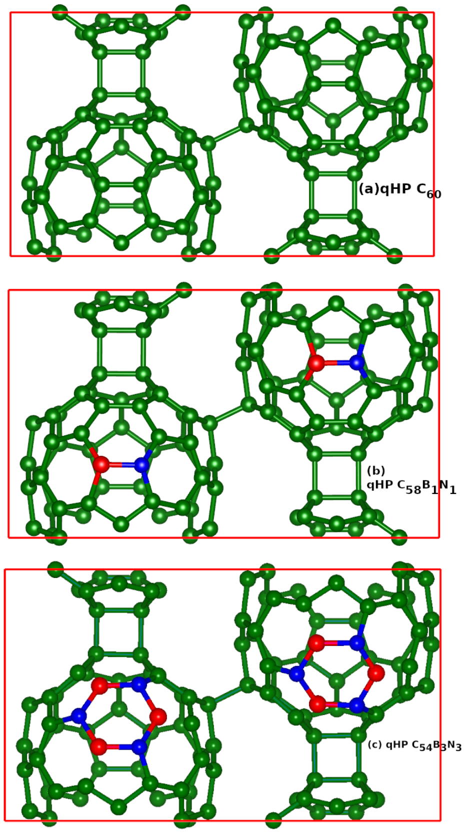

Fig. 1 (a,b) Schematic representation of the optimized atomic configuration of (a) qHP C_{60} (System I), and (b) qHP $C_{58}B_1N_1$ (System II), and c) qHP $C_{54}B_3N_3$ (System III) unit cell. The green, red, and blue balls denote the Carbon, Boron, and Nitrogen atoms.

dominant variations in other properties. The literature also confirmed that the C_{60} polymer exhibits positive frequencies across the Brillouin zone, indicating dynamical stability [13].

3.2 Electronic structure and Chemical reactivity

Strain and defect engineering are powerful techniques for tailoring the optoelectronic properties of two-dimensional (2D) materials. However, the interaction between mechanical strain and defects in these systems is poorly understood [35]. Strain engineering, or "straintronics," has proven particularly effective for 2D materials due to their ability to endure significant elastic strain before deformation or fracture. For instance, graphene can withstand up to 18% elastic strain [36], while MoS2 can handle up to 11% [37]. We examined the impact of low defect concentrations under external axial tensile strain along 2D plane. Although compressive strain is possible, significant values are unlikely due to the tendency of 2D materials to buckle or fold. Therefore, we simulated the effects of small compressive/expansion strain up to $\pm 2.0\%$. In Figure 2(a,b,c), we have demonstrated the variation in bandgap as a function of applied strain (both compression and expansion) along the x- and y directions.

The effect of strain on qHP C_{60} and qHP $C_{54}B_3N_3$ shows similar behaviour compared to qHP $C_{58}B_1N_1$ sheet. This anomaly arises as the cyclic arrangement of three BN pairs provides an environment equivalent to three CC pairs (iso-electronic). On applying negative strain, the bandgap for system II shows a large deviation compared to systems I and III. In contrast, applying positive strain along the x-axis leads to a decrease in band gap for systems I and III, but for system I, it increases then decreases. The band gaps of fullerene monolayers decrease roughly linearly with increasing tensile strain. However, their band gaps' response to compressive strain is non-linear, as the conduction band maximum shifts among various high-symmetry k-points. Additionally, the effective masses of electrons and holes show significant anisotropy and can be adjusted by applying compressive and tensile strains. This suggests that the monolayer of doped BN fullerene sheets holds considerably better potential for device modelling applications.

Figure 3 presents the calculated band structures and total density of states (DOS) for qHPs for (a) C_{60}, (b) $C_{58}B_1N_1$, and (c) $C_{54}B_3N_3$. All three systems display a direct bandgap with the valence band maximum (VBM) and conduction band minimum (CBM) at the Γ-point of the Brillouin zone, showing significant band dispersion. The parabolic nature of the CBM and VBM in qHP $C_{58}B_1N_1$ indicates the applicability of the deformation potential theory compared to the other two structures, which have comparatively flat bands. In a recent study, the qTP structures of fullerene and its similar doped counterparts demonstrate VBM and CBM located at Γ and X -point of the Brillouin zone with an indirect band gap [34]. There appears to be a slight mismatch between the band structure and DOS in Figure 3. This minor discrepancy is due to the smearing applied to the NSCF calculations, which helps to smooth the DOS and eliminate wrinkles in the curve. Due to the known underestimation of bandgaps by DFT with the PBE functional [38,39], the HSE functional was also used for accurate bandgap determination. The bandgaps calculated us-

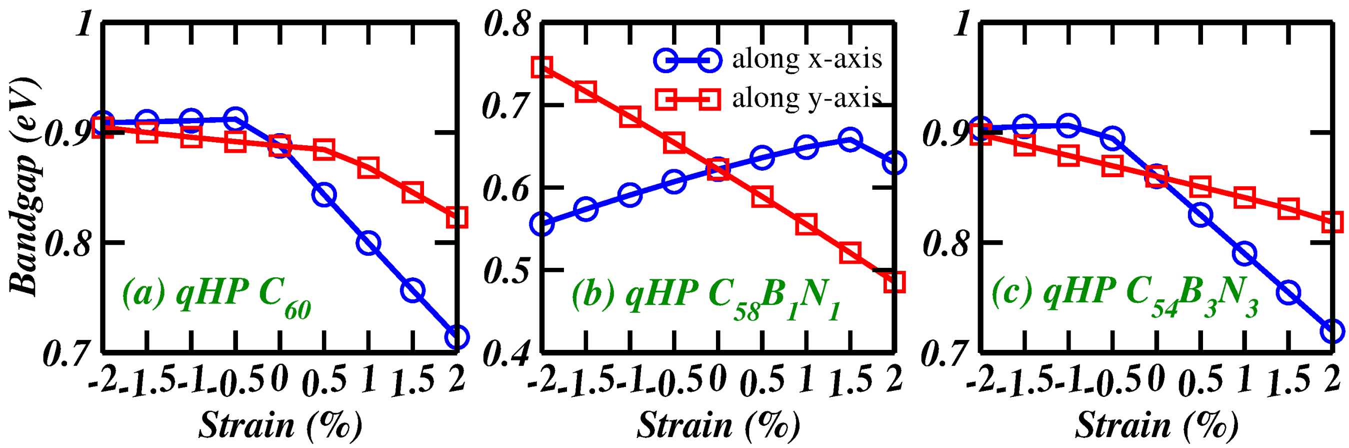

Fig. 2 Bandgap Vs Strain plot for (a) qHP C_{60}, and (b) qHP $C_{58}B_1N_1$ systems, respectively.

	Systems		
Properties	qHP C_{60}	qHP $C_{58}B_1N_1$	qHP $C_{54}B_3N_3$
Lattice parameter **a**(Å)	15.87	15.87	15.84
Lattice parameter **b**(Å)	9.14	9.14	9.14
Cohesive Energy E_{coh}(eV)	-8.75	-8.70	-8.67
HOMO (eV)	-1.03	-0.87	-0.87
LUMO (eV)	-0.14	-0.25	-0.01
E_{gap} (HSE) (eV)	0.89(1.46)	0.62(1.07)	0.86(1.47)
E_{fermi} (eV)	-0.63	-0.56	-0.48
Chemical Potential μ(eV)	-0.59	-0.56	-0.44
Hardness η (eV)	0.44	0.31	0.43
Softness **S**(eV^{-1})	0.22	0.16	0.22
Electrophilicity ω (eV)	0.08	0.05	0.04
Elastic Constant C_{2D}[C_{11}(C_{22})]	438.01(459.26)	430.03(452.18)	423.60(452.56)
Conductivity σ/τ at 300K	2.59x10^{10}	9.80x10^{12}	5.09x10^{10}
Work function (eV)	4.91	4.82	4.78

Table 1 Lattice parameter (Å), Cohesion energy E_{coh} (eV), HOMO energy (eV), Fermi Level (eV), LUMO energy (eV), Band gap E_{gap} (eV), Chemical Potential μ (eV), Hardness η (eV), Softness S (eV), Electrophilicity ω (eV), Elastic Constant ($N/m(Jm^{-2})$), Conductivity ($\Omega^{-1}cm^{-1}s^{-1}$), and work function (eV) for (a) qHP C_{60}, (b) qHP $C_{58}B_1N_1$, and (c) qHP $C_{54}B_3N_3$, respectively.

ing PBE (HSE) were 0.89 eV (1.46 eV) for qH C_{60}, 0.62 eV (1.07 eV) for qHP $C_{58}B_1N_1$, and 0.86 eV (1.47 eV) for qHP $C_{54}B_3N_3$, as shown in Figure 4.

From HSE results, one can predict that both qHPs of C_{60} and $C_{54}B_3N_3$ systems exhibit a wider bandgap semiconductor ($\sim$ 1.5 eV) whereas qHP-$C_{58}B_1N_1$ demonstrate bandgap in the range of 1.0 eV. It is well known that Silicon, which has revolutionized the micro-electronic industry, exhibit an indirect bandgap ($\sim$1.50 eV). Herein, we showed that both the BN doped C_{60} sheets exhibit an interesting material that shows a range of bandgap very close to that of Silicon. Based on the bandgap, we conclude that these doped materials can be used for future nano- and optoelectronic devices (as the band gap is below 2.0 eV). We also examined the total and partial density of states (PDOS) of all three systems, shown in Figure SI 4. From the PDOS, it is apparent that qHP $C_{58}B_1N_1$ have a smaller bandgap than the other two systems, matching well with band structure and bandgap calculations. As our systems are carbon-rich, it is observed that both CBM and VBM are dominated by Carbon p-orbital in all three cases.

Doping in 2D materials significantly alters their chemical reactivity by introducing foreign atoms or molecules into the lattice, modifying electronic properties, and creating active sites. This can enhance catalytic activity, tailor band gaps, and improve sensor performance. Consequently, calculating comprehensive descriptive DFT parameters like chemical potential μ [40], global softness (S), global hardness η [41], and electrophilicity ω [42] provide an effective method for understanding the effects of doping on chemical reactivity. The equations are as follows:

$$\mu = \frac{E_{HOMO} + E_{LUMO}}{2}$$
$$\eta = \frac{E_{LUMO} - E_{HOMO}}{2}$$
$$S = \frac{1}{2\eta} \tag{3}$$
$$\omega = \frac{\mu^2}{2\eta}$$

The results based on equations 3 are given in Table 1. Incorporating dopants has broadened the range of applications for these nanosheets, making them suitable for use in areas such as batteries, medical, and other semiconducting devices. HOMO/LUMO results (not displayed) for the doped systems indicate that charge accumulation or depletion primarily occurs around the BN site. This makes it an ideal location for adsorption and catalysis. [16,34].

3.3 Mechenical and optical properties

The elastic constants of solids are significant for both fundamental and practical reasons. Fundamentally, elastic constants represent the second derivatives of a thermodynamic potential concerning strain, directly linking them to atomic bonding and structure (Federov 1968) [43]. They provide critical information about a material's stability, stiffness, brittleness, ductility, and anisotropy. The elastic modulus (C_{2D}) for longitudinal strain in the x and y directions of the longitudinal acoustic wave is calculated using parabolic fitting of the equation $(E-E_0)/S_0 = C_{2D}\varepsilon^2/2$, where E is the total energy of the deformed system, E_0 is the equilibrium energy, and S_0 is equilibrium area. Strain is applied in both directions (xy plain), ranging from -2% to +2%. The computed elastic constants C_{2D} in units of Jm^{-2} are 438.01 (459.26), 430.03 (452.18), and 423.60 (452.56) along the x (y) direction for qHP's of C_{60}, $C_{58}B_1N_1$, and $C_{54}B_3N_3$, respectively. For comparison, the experimental and theoretical elastic constants (C^{β}) are 260 J/m² for BN, 350 Jm^{-2} for graphene, and 385 J/m² for qTP C_{60}, indicating their strain-induced stability [44–46].

The conductivity of the given systems was determined using semiclassical Boltzmann theory within the constant relaxation time approximation, employing the BoltzTrap code [47]. Using the BoltzTrap code, conductivity and mobility can be obtained only under the relaxation time approximation. In this approach, the conductivity is calculated using the equation

$$\sigma_{\alpha,\beta}(T,\nu) = \Sigma_i \int \frac{dk}{8\pi}[-\frac{\partial f(T,\nu)}{\partial \varepsilon}]\sigma_{\alpha,\beta}(i,k) \tag{4}$$

Here f is the Fermi-Dirac distribution function, and ν is the chemical potential determined by the number of free carriers. The conductivity tensor is given $\sigma_{\alpha,\beta}(i,k) = e^2\tau_{i,k}v_{\alpha}(i,k)v_{\beta}(i,k)$, where $v(i,k) = \hbar^{-1}\frac{\partial \varepsilon_{i,k}}{\partial k_{\alpha}}$ represents the group velocity of i^{th} band for α component. From the figure 5, it is apparent that $C_{58}B_1N_1$ shows conductivity (σ/τ) behaviour at lower temperature as compared to C_{60} and $C_{54}B_3N_3$. The computed values of conductivity of qHP's of C_{60}, $C_{58}B_1N_1$ and $C_{54}B_3N_3$ at 300 K are 2.59×10^{10}, 9.80×10^{12}, and 5.09×10^{10}, in units of $\Omega^{-1}cm^{-1}s^{-1}$, respectively. Here It was found that qHP $C_{58}B_1N_1$ shows a thousand times (× 1,000) higher conductivity compared to the other two systems. Interestingly the qHP $C_{54}B_3N_3$ also shows higher conductivity compared to qHP C_{60}. In previous work on qTP C_{60} and its similar doped systems, the conductivity at 300 K for $C_{54}B_3N_3$ is found to be zero and only shows conductivity at higher temperature [34]. It can be concluded that replacing a CC pair with a BN pair in the C_{60} fullerene sheet significantly affects the system's conductivity due to the generation of polarity into the bond.

The work function (Φ) of all the compounds is calculated using the equation $\Phi = E_{vaccum} - E_{fermi}$, which represents the energy needed to remove an electron from the Fermi level to a point far away in the vacuum. The work function is a crucial parameter in surface science, catalysis, and related fields, as it characterizes a given surface. The computed work function of the pristine qHP C_{60} is 4.91 eV, demonstrating good congruence with the experimental value of 4.56 eV [48?] for graphene and 4.85 qTP C_{60}. The work function for qHP of $C_{58}B_1N_1$ and $C_{54}B_3N_3$ is found to be 4.82 eV and 4.78 eV, respectively and is shown in Figure SI 4. The work function of impurity-doped graphene varies depending on the concentration of the impurity defects. [48].

The frequency-dependent complex dielectric constant was calculated using Density Functional Theory (DFT) within the random phase approximation (RPA) [49]. This calculation assesses and characterizes the optical properties of materials. The real (ε_1) and imaginary (ε_2) parts of the dielectric function (ε) were com-

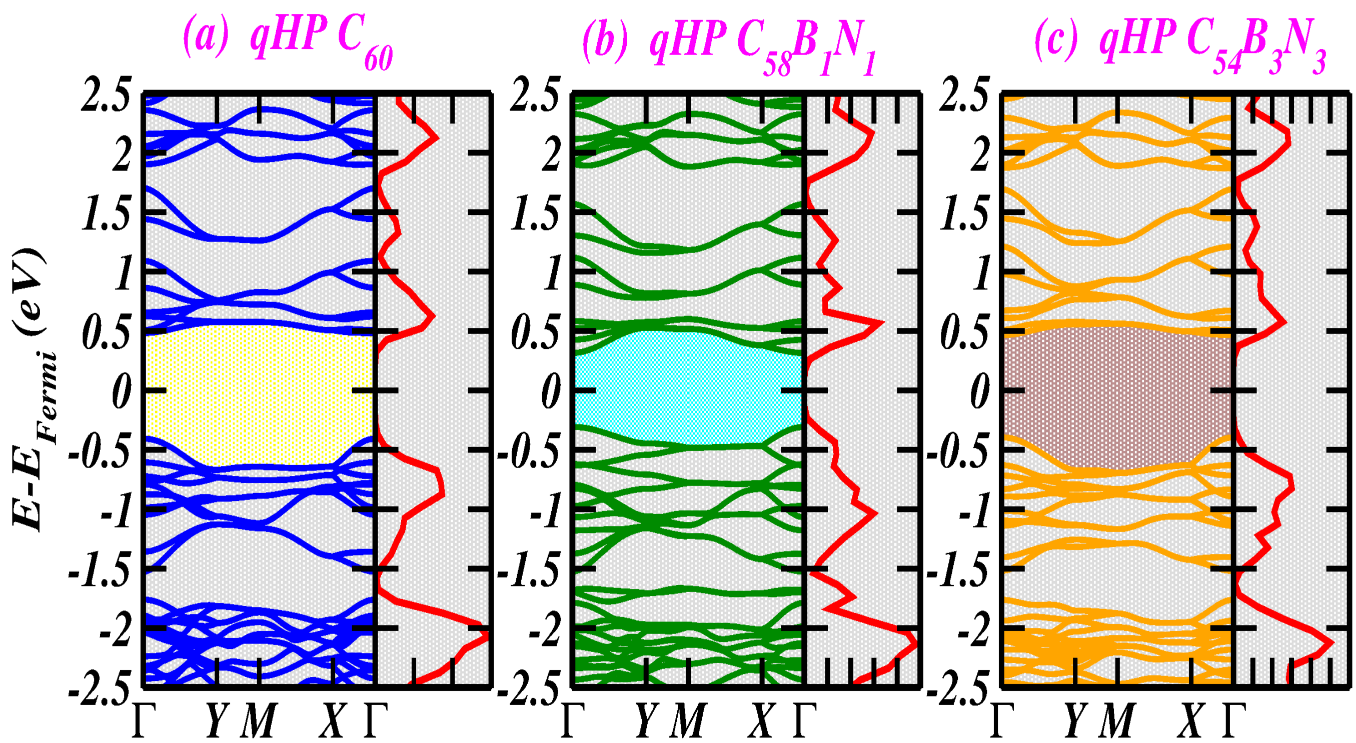

Fig. 3 The calculated band structures and total density of states (DOS) for (a) qHP C_{60}, and (b) qHP $C_{58}B_1N_1$, respectively.

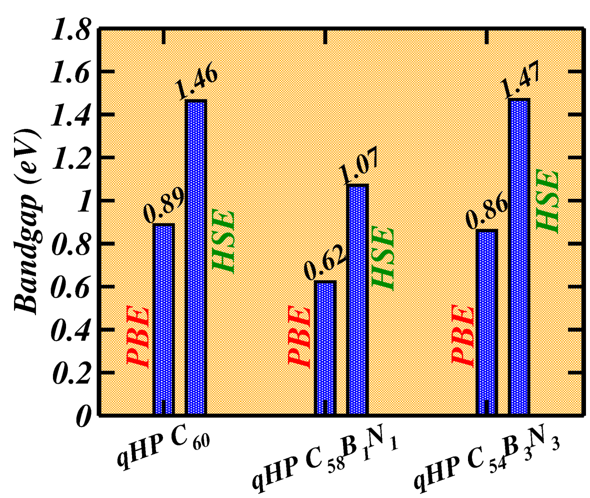

Fig. 4 Band gap of qHP of C_{60}, $C_{58}B_1N_1$, and $C_{54}B_3N_3$ using PBE and HSE functional, respectively.

puted using relevant equations (Equation No. 5) [34,50–53]. This complex dielectric constant is crucial for understanding optical characteristics such as optical absorption, electron energy loss spectra, refractivity, extinction coefficient, reflectivity, and transmittance [54,55].

$$\varepsilon(\omega) = \varepsilon_1(\omega) + \varepsilon_2(\omega)$$

$$\varepsilon_1(\omega) = 1 + \frac{2}{\pi} p \int_0^{\infty} \frac{\omega' \varepsilon_2(\omega') d\omega'}{(\omega'^2 - \omega^2)} \tag{5}$$

$$\varepsilon_2(\omega) = \frac{4\pi^2 e^2}{m^2 \omega^2} \sum_{ij} \int_k \langle i|M_j\rangle^2 f_i(1-f_i) X \delta(E_{jk} - E_{ik} - \omega) d^3k$$

Figure 6 displays the real and imaginary parts of the dielectric constant for monolayers C_{60}, $C_{58}B_1N_1$, and $C_{54}B_3N_3$. The real part, which indicates electronic polarizability, can be determined using the Clausius-Mossotti relation [53]. It provides insights into the material's electronic polarizability. The static dielectric function, or optical dielectric constant, refers to the real part at zero photon energy. The imaginary part corresponds to the inter-band transition of electrons from the valence to the conduction band. Figure 6 (a,b,c) shows that the static dielectric constant is approximately 4.07, 4.24, and 3.88 eV for in-plane ($E||X$) and around 2.55, 2.64, and 2.49 eV for out-of-plane ($E \perp Z$) polarization. This data indicates anisotropic optical properties, with greater electronic polarization along the in-plane direction. Notably, a negative value around 4.25 ($\pm$ 0.50) eV at $E||X$ for all three qHP systems suggests metallic characteristics at this photon energy, but it does not show any metallic character along $E \perp Z$ polarization. In contrast, this metallic character completely vanished in

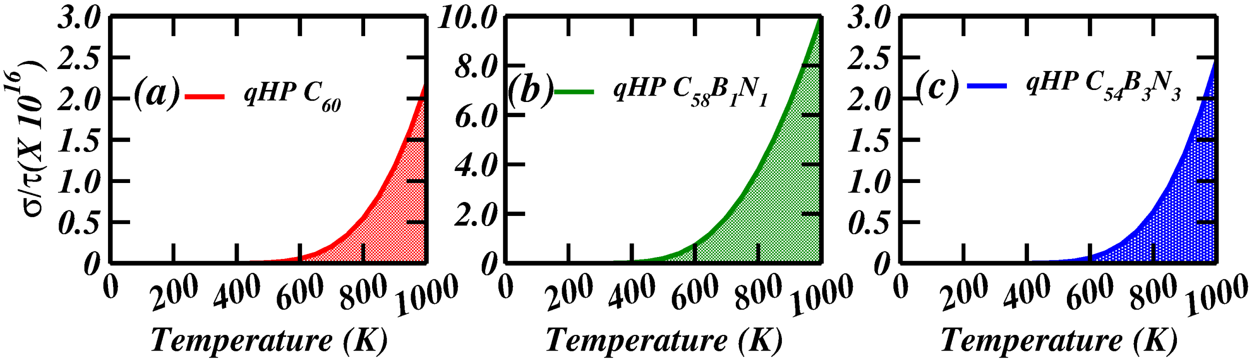

Fig. 5 Conductivity in units of $(\Omega^{-1}cm^{-1}s^{-1})$ as a function of temperature, (a) qHPC_{60}, and (b) qHP $C_{58}B_1N_1$, respectively.

the qTPs of $C_{58}B_1N_1$ and $C_{54}B_3N_3$ shows no negative values neither in $E||X$ nor in $E \perp Z$ polarization [34]. Significant peaks (maxima) occur at 6.58 (3.41) eV, 5.64 (3.19) eV, and 5.54 (3.26) eV for $E||X$ ($E \perp Z$) and maximum electronic polarizability is identified at 1.20 (0.90, 1.20) eV ($E||X$) and 1.30 (0.85, 1.35) eV ($E \perp Z$) for qHPs of C_{60} ($C_{58}B_1N_1$ and $C_{54}B_3N_3$), respectively. Figure 6(d,e,f) presents the imaginary part of the dielectric function associated with interband transitions. In the low-frequency range, it shows the minimal response to electromagnetic radiation up to about 1.80(1.25, 1.85) eV for parallel and 1.81(1.55, 1.85) eV for perpendicular polarization in qHPs of C_{60} ($C_{58}B_1N_1$ and $C_{54}B_3N_3$). This agrees with the Density of States (DOS) analysis in Figure 4 (HSE results), indicating no interband transitions from the Valence Band Maximum (VBM) to the Conduction Band Minimum (CBM) within the bandgap.

Figure 7 (a) shows the frequency-dependent absorption coefficient averaged across three electric field orientations, which is crucial for assessing optical properties in optoelectronic applications. The absorption coefficient ($\alpha(\omega)$) measures light intensity attenuation over a unit distance as an electromagnetic wave propagates through a medium. It is directly related to the imaginary part of the dielectric function and the extinction coefficient, as shown in Figure 6(d,e,f). A lower absorption coefficient indicates less light absorption by the material. For all three systems, the first absorption peak appears between 1.0-2.0 eV, with the highest peak around 5.1 and 11.20 eV in the UV region. The absorption coefficient is minimal at lower energies ($\sim$ 1.5 eV). The high ($\alpha(\omega)$) value of $\sim 4.11x10^5cm^{-1}$ potential use of C_{60}, $C_{58}B_1N_1$, and $C_{54}B_3N_3$ monolayers as UV absorbers.

The energy loss function $L(\omega)$ is depicted in Figure 7(b). Multiple distinct peaks are evident at approximately 1.6 eV, 6.02 eV, and 11.40 eV for the electric field aligned parallel to the single layer of all sheets. These peaks correspond to the $(\pi+\sigma)$(plasmon excitation. Conversely, there are no noticeable peaks at energy levels below 0.9 eV for parallel or perpendicular polarizations. A few faint peaks are observed within the energy range of 1.0 eV to 1.5 eV, attributed to subtle resonances of incident light. For the proposed monolayers, the plasmonic peaks experience a shift toward higher energies and display increased sharpness (blueshift) when the material reflects frequencies of electromagnetic radiation below the plasma frequency. This phenomenon occurs because the electrons within the substance effectively shield the electric field of the radiation. Conversely, if electromagnetic radiation surpasses the plasma frequency, it is transferred through the material when the electrons within it cannot shield it [57–59].

3.4 Photo-electro catalysis

Two-dimensional materials have been extensively researched as catalysts for hydrogen generation over the past two decades due to their exceptional catalytic properties and unique atomic structure [16,34,60]. This study investigated these compounds' hydrogen evolution reaction (HER) and oxygen evolution reaction (OER) activities, focusing on their suitable band gaps. It is well-known that an attractive semiconductor for HER/OER must have band edges that align with the redox potentials of water. Specifically, the valence band maximum (VBM) should be more positive than the H_2O/H_2 level. The conduction band minimum (CBM) should be more negative than the H_2O/O_2 level, ensuring favourable water-splitting energetics without needing an applied bias voltage. To design an efficient photo-catalyst for water-splitting, it is crucial to determine the semiconductor's band edge positions relative to the H_2O/O_2 and H_2O/H_2 levels in water. A straightforward approach involves calculating these band edge positions relative to a standard reference, typically the vacuum level. The standard redox potentials of water are -4.44 eV for reduction H_2O/H_2 and -5.67 eV for oxidation H_2O/O_2 using the vacuum level as a reference. Thus, the positions of the valence and conduction bands relative to the vacuum potential of the respective sheets were determined using the equations $E^{VBE/CBE} = E^{VBM/CBM} - E_{vacuum}$. In all three C_{60} configurations studied, the Fermi energy (E_{fermi}) is around -0.60 eV, leading to an overpotential of about 4.28 eV relative to the HER redox potential. Figure 8 shows that by employing PBE functional, the HER potential lies within the bandgap, highlighting the ability of C_{60} and $C_{54}B_3N_3$ sheets to reduce H^+ to H_2, thus presenting new possibilities in electrocatalysis. Whereas results based on HSE functional demonstrate that all three systems can reduce H^+ to H_2. HSE results also indicate that C_{60} has the potential for Oxygen Evolution Reaction (OER) activity. Based on HSE calculation, these systems' valence and conduction band edges effectively straddle the HER redox potential, suggesting their potential as metal-free electrocatalysts. Overall, HSE functional calculations indicate that the electronic structures of these systems favour their HER activity.

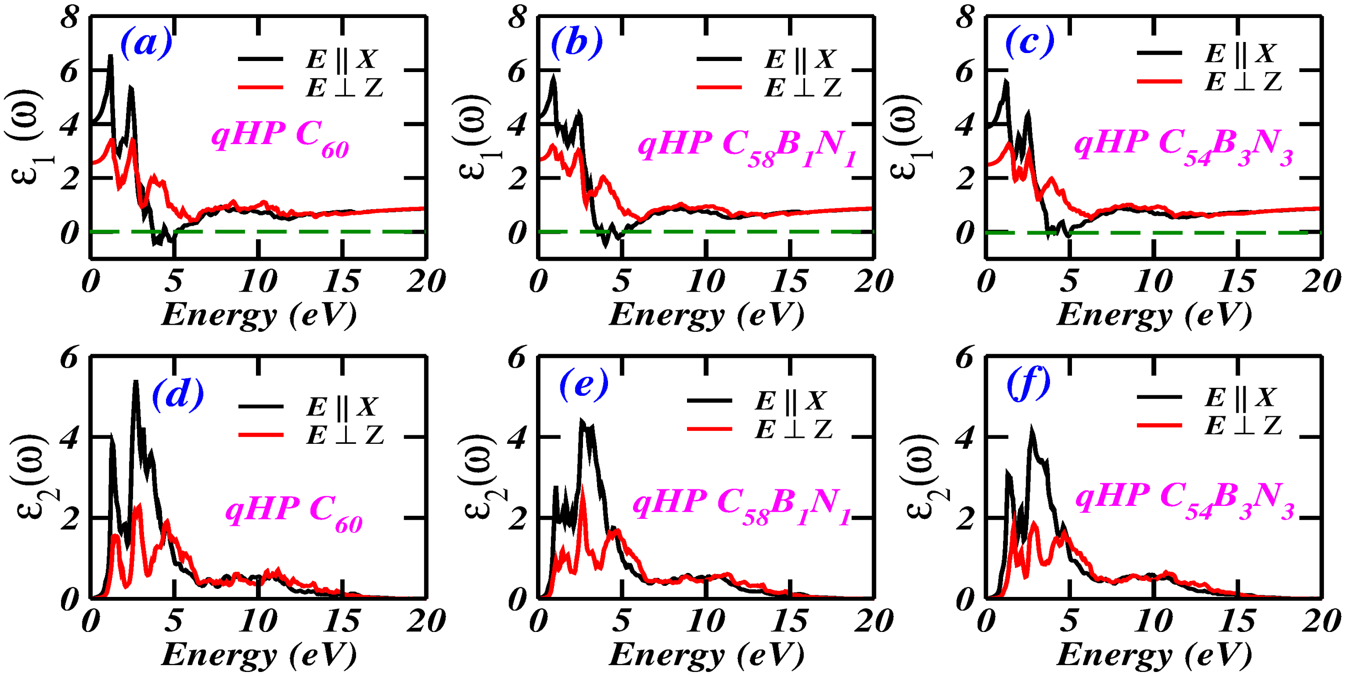

Fig. 6 (a,b,c) Real (ε_1) and (d,e,f) imaginary (ε_2) dielectric function, of monolayers qHP C_{60}, qHP $C_{58}B_1N_1$, and qHP $C_{54}B_3N_3$, respectively.

Given that BN-doped C_{60} can potentially replace Pt-based electrocatalysts, careful manipulation of its bandgap through defect engineering (e.g., altering the BN arrangement) could lead to the development of efficient non-metal photo- and electro-catalysts for HER.

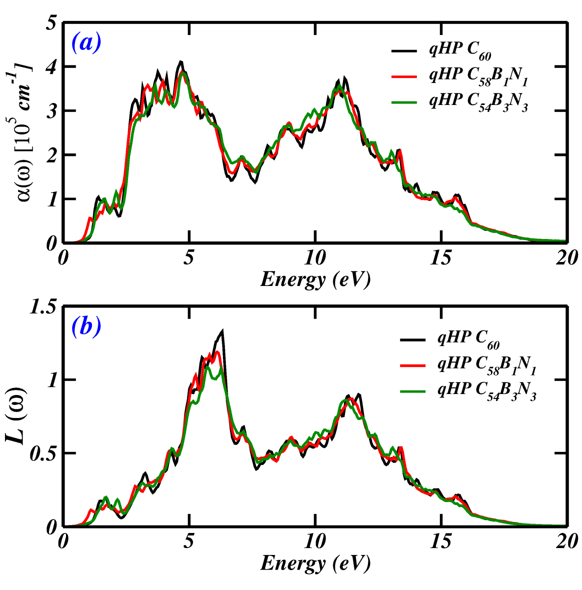

Fig. 7 (a) Absorption coefficient (α) and (b) electron energy loss spectrum (L) of qHP monolayers of C_{60}, $C_{58}B_1N_1$, and $C_{54}B_3N_3$, respectively.

3.5 Classical Molecular Dynamics Simulations

As mentioned that the classical molecular dynamics (MD) simulations could analyze the thermal stability and structural transformation of qHPC_{60}, qHP$C_{58}B_1N_1$ and qHP$C_{54}B_3N_3$, we plot the total-energy at various temperatures in Figure 9 (a). The curve for the qHPC_{60} (black line), is lower in energy than qHP$C_{58}B_1N_1$ and qHP$C_{54}B_3N_3$ indicating its greater stability. The higher stability of pristine qHPC_{60} is also supported by our first-principles simulation results predicting its notably higher negative formation energy value. However, the qHPC_{60}, qHP$C_{58}B_1N_1$ and qHP$C_{54}B_3N_3$ show similar trend for the drop in their energies. Each curve in Figure 9 (a) can be divided into three regions based on the slope: before the jump in the total energy (I), the jump itself (II) and after the jump (III). Region I corresponds to the phase where the qHPC_{60} cages are a bit structurally deformed as the temperature rises, as shown in Figure S1(a-b), S2(a-b) and S3(a-b). In this wide range, it contains large numbers of local configurations of pentagons, hexagons and heptagons, etc., which keeps the overall number of C−C bonds unchanged. As a result, the system's total energy does not increase sharply with temperature. The region where larger rings were lost and linear atomic chains (LACs) formed before the lattice atomization started occurring in Region (II). The qHPC_{60} system begins to lose structural integrity, signalling the onset of the melting process at around 3900K. This causes the cage to rupture and unravel, as shown in Figures S1(c), S2(c) and S3(c). At the final stage, Region III

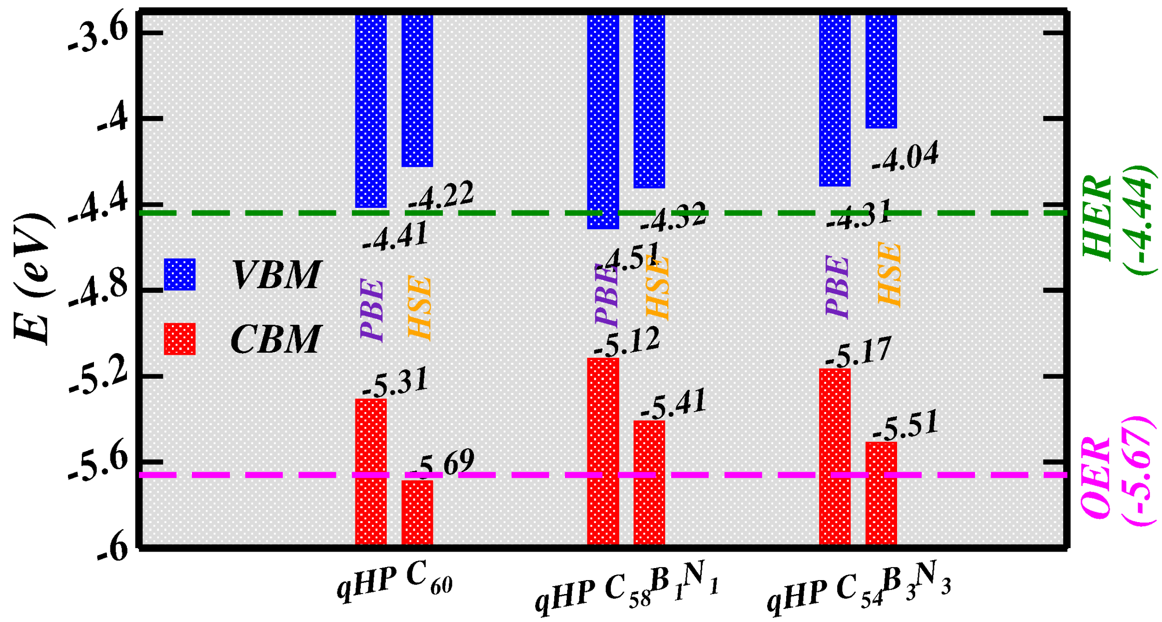

Fig. 8 Band-edge energies of valence (red) and conduction (green) band edges of the C_{60}, $C_{58}B_1N_1$, and $C_{54}B_3N_3$ configurations. A green and magenta dashed line denotes the energy level for the hydrogen evolution reaction (HER) and Oxygen Reduction Reaction (ORR).

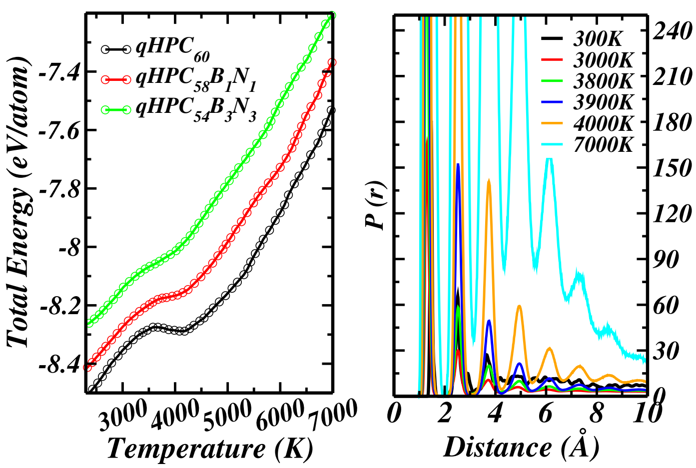

Fig. 9 (a) Temperature dependence of total energy when melting qHPC_{60}, qHP$C_{58}B_1N_1$ and qHP$C_{54}B_3N_3$ at different temperatures. (b) Radial distribution function carried out at different temperatures for qHPC_{60}.

with T > 3900 K [See Figs. S1(d)-S2(d)], the phase transition occurs corresponding to the gaseous phase of the system where only atoms/short atomic chains are observed. The system looks uniform, as it should be in gas, leading to a sharp energy increase. It is important to note that the melting temperature of qHPC_{60} at $\sim$ 3900 K is comparable to those from [61], where sublimation was observed using reactive force field ReaxFF, and a bit lower than the monolayer graphene (4095K) [62]. While, the melting process for qHPC_{60} at all the stages is similar to qHP$C_{54}B_3N_3$ and qHP$C_{58}B_1N_1$, but the melting temperature of qHPC_{60} is negligibly higher than the doped ones as evident from the slow decay of Region II in qHPC_{60} Figure 9. The morphology evolution is consistent with the change in the local structure as shown by the radial distribution function (RDF) for qHPC_{60} in Figure 9 (b). It should be mentioned that the trend of RDFs for qHP$C_{58}B_1N_1$ and qHP$C_{54}B_3N_3$ is similar to the ones shown here for qHPC_{60}. At room temperature of 300K, the black curve with a lot of maxima and minima is the characteristic of a perfect crystalline-like system. The first few maxima of RDFs decrease but get broader as the temperature is raised. At moderate temperatures before 3000K, the minima of RDFs fall almost to zero when the melting process starts around 3800K. During melting, as evident from RDF at 3900K, the third minimum possesses a finite value, determining the loss of rings and formation of LACs. We observe a smoothening and steady loss in the few peaks of pair correlation as the temperature is further raised to 7000K. At 7000 K, the system is almost melted and on the way to becoming a gas phase supported by the snapshots of atomization at 7000K. [See Fig.S1(d), S2(d) and S3(d)]. The stress response as a function of the uniaxial applied strain is presented in Figure 10 when subjected to temperature regimes ranging from 300K to 900K, considering a uniaxial strain applied in y-directions here. As can it can be perceived, they were stretched at a constant rate where these materials initially show a well-defined (linear) elastic region until total rupture. Young's modulus is defined as the slope of the linear part of this stress-strain curve, while the fracture stress is the point where the peak stress is reached. In our calculations, 5 % of strain is used to estimate Young's modulus values for qHPC_{60}, qHP$C_{58}B_1N_1$ and qHP$C_{54}B_3N_3$: 181.22 GPa, 176.08 GPa and 187.35, respectively as mentioned in Table 2. The results of graphene and hexagonal Boron Nitride are also provided in Table 1 as we performed extra simulations to reproduce and to compare our results with the previous literature values [61]. Although these values are much lower than graphene and hBN structures, they are comparable to previous results of qHPC_{60} [61]. It is very much obvious that increasing the temperature from

Systems	Fracture Stress (GPa)	Young Modulus (GPa)
graphene	121.14	953.93
h-BN	105.55	697.66
qHP C_{60}	33.11	181.22
qHP $C_{58}B_1N_1$	34.99	176.08
qHP $C_{54}B_3N_3$	37.87	187.35

Table 2 Comparison of the fracture stress and Young's modulus for graphene, qHPC60 and its associated structures.

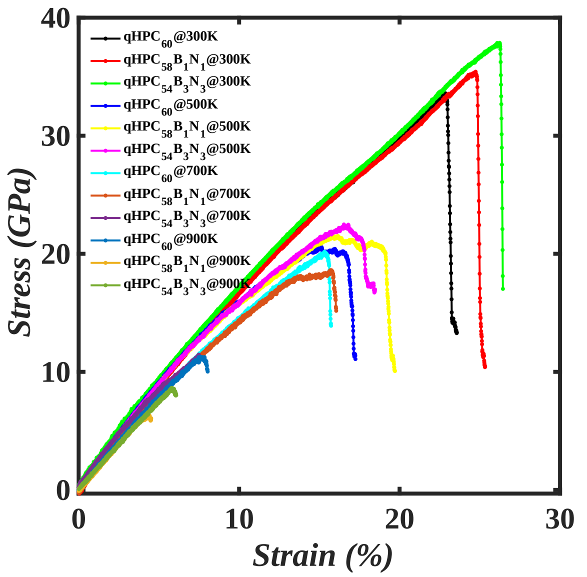

Fig. 10 (a,b) The tensile stress–strain curves for qHPC_{60} , qHP$C_{58}B_1N_1$ and qHP$C_{54}B_3N_3$ at different temperatures.

300K to 900K, there is a decrease in the critical tensile strain values for qHPC_{60}, qHP$C_{58}B_1N_1$ and qHP$C_{54}B_3N_3$, respectively. (Figure 10). It is to note that at 300K and 600K, the stress-strain curves for qHPC_{60} decay faster than the doped counterpart, indicating the lesser stiffness of qHPC_{60} at near equal to room temperatures. But, as evident from higher temperature stress-strain curves, qHPC_{60} decays at a larger stress value than qHP$C_{58}B_1N_1$. This is due to the easy breakage of the more polarized B-N bond at higher temperatures than the C-C bond. These results indicate that the qHPC_{60} may bear lesser stress at room temperature but it could tolerate the higher stress than the doped counterpart at the higher temperatures.

4 Conclusions

This study explored the structural, chemical, electrical, and optical characteristics of pristine C_{60} nanosheets, along with the effects of BN doping. Using quantum mechanical DFT calculations and classical molecular dynamics simulations, we found that all studied structures displayed significant negative cohesion energies, indicating their energetic stability. Both doped and pristine nanosheets were stable. Our global descriptor-DFT parameters showed the order of chemical reactivity as $C_{58}B_1N_1$ > $C_{54}B_3N_3$ > C_{60}, suggesting a degree of chemical reactivity in all nanostructures. The analysis of the HOMO-LUMO gap and PDOS revealed that both pristine and BN-doped C_{60} nanosheets are semiconductors with bandgap ranges from 1.0-2.0 eV. Optical properties, including electron absorption spectra and circular dichroism, confirmed the optical activity of all nanosheets. Our classical MD simulations showed high mechanical strength and good thermal stability for qHP C_{60} and BN-dopedC_{60} systems. This comprehensive study highlights the diverse properties of C60 nanosheets and the influence of BN doping, suggesting their potential use in photovoltaic devices and 2D field-effect transistors. Future research will include ab initio calculations with more reliable hybrid functionals and different dopants to design efficient semiconducting materials for catalysis and optoelectronic devices.

5 Data availability

The data for this study primarily consists of the input files used in our computational models. Given the nature of our work, the critical aspects of our findings are derived from these input files rather than extensive raw datasets. We are more than willing to share these input files with interested researchers upon reasonable request.

6 Author Contributions

SY, SS, and VKY performed calculations, analysed the results and wrote the manuscript.

7 Acknowledgment

SY acknowledge National Supercomputing Mission (NSM) for providing computing resources of 'PARAM Shivay' at Indian Institute of Technology (BHU), Varanasi, which C-DAC implements and supported by the Ministry of Electronics and Information Technology (MeitY) and the Department of Science and Technology (DST), Government of India. S.S. acknowledges VIT Bhopal for providing MATLAB to perform the calculations. VKY sincerely thanks the University of Allahabad for providing a computational facility.

8 Keywords

Density functional theory (DFT), qHP C_{60} fullerene network, BN doping, Optical properties, HER activity, Conductivity.

9 Supplementary Information

Refer to the supplementary material for plots to derive structures of pure and BN-doped C_{60} polymeric 2D sheets, benchmarking plot of energy Vs k-point, plots for PDOS and work functions, MD Snapshot of structures for all three systems at 300 to 7000 K temperatures, QE input files for all the three systems.

References

1 Novoselov KS, Geim AK, Morozov SV, et al. Discover of graphene: electric field effect in atomically thin carbon films. Science (2004)306, 666, doi:10.1126/science.11028.

2 K.S. Novoselov, A.K. Geim, S.V. Morozov, D. Jiang, M.I Katsnelson, I.V. Grigorieva, S.V. Dubonos, A.A. Firsov, Two-dimensional gas of massless Dirac fermions in graphene, Nature 2005, 438, 197.

3 Antiochia R, Tortolini C, Tasca F, et al. Graphene and 2D-like nanomaterials: different biofunctionalization pathways for electrochemical biosensor development. Graphene Bioelectron. 2018: :1–35. doi:10.1016/B978-0-12-813349-1.00001-9.

4 F. Ruhao, X. Cui, M.A. Khan, C. Stampfl, S.P. Ringer, Rongkun Zheng, Strain-Engineered Ultrahigh Mobility in Phosphorene for Terahertz Transistors. Advanced Electronic Materials (2019) 1800797.

5 Hou, L., Cui, X., Guan, B. et al. Synthesis of a monolayer fullerene network. Nature 2022, 606, 507–510. https://doi.org/10.1038/s41586-022-04771-5

6 Kim, K.; Larentis, S.; Fallahazad, B.; Lee, K.; Xue, J.; Dillen, D. C.;Corbet, C. M.; Tutuc, E. Band Alignment in WSe2-Graphene Heterostructures. ACS Nano 2015, 9, 4527-4532.

7 Zhang, C.; Gong, C.; Nie, Y.; Min, K.-A.; Liang, C.; Oh, Y. J.; Zhang, H.; Wang, W.; Hong, S.; Colombo, L.; Wallace, R. M.; Cho, K. Systematic study of electronic structure and band alignment of monolayer transition metal dichalcogenides in Van der Waals heterostructures. 2D Materials 2017, 4, 015026.

8 Yu, Z. G.; Zhang, Y.-W.; Yakobson, B. I. Strain-Robust and Electric Field Tunable Band Alignments in van der Waals WSe2-Graphene Heterojunctions. J. Phys. Chem. C 2016, 120, 22702-22709.

9 Pierucci, D.; Henck, H.; Avila, J.; Balan, A.; Naylor, C. H.; Patriarche, G.; Dappe, Y. J.; Silly, M. G.; Sirotti, F.; Johnson, A. T. C.; Asensio, M. C.; Ouerghi, A. Band Alignment and Minigaps in Monolayer MoS2-Graphene van der Waals Heterostructures. Nano Lett. 2016, 16, 4054-4061.

10 Hill, H. M.; Rigosi, A. F.; Rim, K. T.; Flynn, G. W.; Heinz, T. F. Band Alignment in MoS2/WS2 Transition Metal Dichalcogenide Heterostructures Probed by Scanning Tunneling Microscopy and Spectroscopy. Nano Lett. 2016, 16, 4831-4837.

11 Mei-Yan Gao, Fei Wang, Zhi-Gang Gu, De-Xiang Zhang, Lei Zhang, and Jian Zhang Fullerene-like Polyoxotitanium Cage with High Solution Stability J. Am. Chem. Soc. 2016, 138, 8, 2556-2559

12 Linfeng Yu, Jinyuan Xu, Bo Peng, Guangzhao Qin, and Gang Su, Anisotropic Optical, Mechanical, and Thermoelectric Properties of Two-Dimensional Fullerene Networks, J. Phys. Chem. Lett. 2022, 13, 50, 11622–11629, doi:1.1021/acs.jpclett.2c02702

13 Bo Peng, (a) Monolayer Fullerene Networks as Photocatalysts for Overall Water Splitting, J. Am. Chem. Soc. 2022, 144, 19921-19931; (b) Stability and Strength of Monolayer Polymeric C_{60}, Nano Lett. 2023, 23, 2, 652-658.

14 Durbin, D.; Allan, N.; Malardier-Jugroot, C. Molecular hydrogen storage in fullerenes - A dispersion-corrected density functional theory study. Int. J. Hydrogen Energy 2016, 41, 13116-13130

15 Vivek K. Yadav, Showkat H. Mir, and Jayant K. Singh, A Computational Study of Structural, Electronic and Carrier Mobility of Boron and Phosphorus/Nitrogen Co-doped Graphene; Physica B: Condensed Matter, 571, 291-295 (2019).

16 Vivek K. Yadav, Himanshu Chakraborty, Michael L. Klein, Umesh V. Waghmare, and C.N.R. Rao Defect-enriched tunability of electronic and charge-carrier transport characteristics of 2D Borocarbonitride (BCN) monolayers from ab initio calculations; Nanoscale, 11, 19398-19407 (2019)

17 M Chhetri, S Maitra, H Chakraborty, UV Waghmare, CNR Rao Superior performance of borocarbonitrides, B x C y N z, as stable, low-cost metal-free electrocatalysts for the hydrogen evolution reaction Energy and Environmental Science 9 (1), 95-101

18 LS Panchakarla, KS Subrahmanyam, SK Saha, Achutharao Govindaraj, HR Krishnamurthy, UV Waghmare, CNR Rao Synthesis, structure, and properties of boron-and nitrogen-doped graphene, Advanced Materials 21 (46), 4726-4730 (2009)

19 CNR Rao, K Gopalakrishnan, A Govindaraj Synthesis, properties and applications of graphene doped with boron, nitrogen and other elements Nano today 9 (3), 324-343 (2014)

20 K Raidongia, A Nag, K Hembram, UV Waghmare, R Datta, CNR Rao BCN: a graphene analogue with remarkable adsorptive properties Chemistry-A European Journal 16 (1), 149-157 (2010)

21 Wang J, Durbeej B. How accurate are TD-DFT excited-state geometries compared to DFT ground-state geometries? J Comput Chem. 2020;41(18):1718–1729. doi:10.1002/jcc.26213.

22 L. Wang, Z. Sofer, P. Simek, I. Tomandl, M. Pumera, Boron-Doped Graphene: Scalable and Tunable p-Type Carrier Concentration Doping, J. Phys. Chem. C 117 (2013) 23251-23257.

23 Maroto ESF, Sancho-García JC. Emerging DFT methods and their importance for challenging molecular systems with orbital degeneracy. Computation. 2019;7(4), :62), doi:10.3390/COMPUTATION7040062.

24 Laurent AD, Jacquemin D. TD-DFT benchmarks: A review. Int J Quantum Chem. 2013;113(17):2019-2039), doi:10.1002/qua.24438.

25 P. Giannozzi, S. Baroni, N. Bonini, M. Calandra, R. Car, C. Cavazzoni, D. Ceresoli, G.L. Chiarotti, M. Cococcioni, I. Dabo, et al., QUANTUM ESPRESSO: a modular and open-source software project for quantum simulations of materials, Journal of Physics: Condensed matter 21(39) (2009) 395502.

26 J.P. Perdew, K. Burke, and M. Ernzerhof, Generalized Gradient Approximation Made Simple, Physical review letters 77(18) (1996) 3865.

27 J.P. Perdew, J.A. Chevary, S.H. Vosko, K.A. Jackson,M.R. Ped-

erson, D.J. Singh, C. Fiolhais, Atoms, molecules, solids, and surfaces: Applications of the generalized gradient approximation for exchange and correlation, Physical Review B 46 (1992) 6671.

28 H.J. Monkhorst, J.P. Pack, Special points for Brillouin-zone integrations, Physical Review B 13 (1976) 5188.

29 S. Grimme, J. Antony, S. Ehrlich, H. Krieg, A consistent and accurate ab initio parametrization of density functional dispersion correction (DFT-D) for the 94 elements H-Pu, Journal of Chemical Physics 132 (2010) 154104.

30 J. Heyd, G.E. Scuseria, M. Ernzerhof, Hybrid functionals based on a screened Coulomb potential, Journal of Chemical Physics 118 (2003) 8207-8215.

31 S. Plimpton. Fast parallel algorithms for short-range molecular dynamics, J. Comput. Phys. 117 (1995), 1 https://doi.org/10.1006/jcph.1995.1039

32 W. Humphrey, A. Dalke, and K. Schulten. Vmd: Visual molecular dynamics, Journal of Molecular Graphics 14(1) (1996), 33 https://doi.org/10.1016/0263-7855(96)00018-5

33 Rad AS, Shabestari SS, Jafari SA, et al. N-doped graphene as a nanostructure adsorbent for carbon monoxide: DFT calculations. Mol Phys. 2016;114(11):1756-1762. doi:10.1080/00268976.2016.1145748.

34 Yadav, V. K, Exploring the effect of BN doping in two-dimensional fullerene networks through first principle simulations, FlatChem 2024; 45; 100655

35 Santra, P., Ghaderzadeh, S., Ghorbani-Asl, M. et al. Strain-modulated defect engineering of two-dimensional materials. npj 2D Mater Appl 2024; 8; 33. https://doi.org/10.1038/s41699-024-00472-x

36 Kim, K. S. et al. Large-scale pattern growth of graphene films for stretchable transparent electrodes. Nature 2009; 457; 706-710.

37 Bertolazzi, S., Brivio, J. & Kis, A. Stretching and breaking of ultrathin MoS2. ACS Nano, 2011; 5; 9703-9709.

38 J.P. Perdew, Density functional theory and the band gap problem, Int. J. Quant. Chem. 28 (1985) 497-523.

39 A. Pribram-Jones, D.A. Gross, K. Burke, DFT: A theory full of holes?, Annu Rev. Phys. Chem. 66 (2015) 283-304.

40 Parr RG, Donnelly RA, Levy M, et al. Electronegativity: the density functional viewpoint. J Chem Phys. 1977;68 (8):3801–3807. doi:10.1063/1.436185.

41 Parr RG, Pearson RG. Absolute hardness: companion parameter to absolute electronegativity. J. Am. Chem. Soc. 1983;105(26):7512–7516. doi:10.1021/ja00364a005.

42 Niazi A, Jameh-Bozorghi S, Nori-Shargh D. Prediction of toxicity of nitrobenzenes using ab initio and least squares support vector machines. J. Hazard. Mater. 2008;151(2–3):603–609. doi:10.1016/j.jhazmat.2007.06.030.

43 N.V. Thang, X.F. Miao, N.H. van Dijk, E. Bruck, Structural and magnetocaloric properties of (Mn,Fe)2(P,Si) materials with added nitrogen; Journal of Alloys and Compounds 2016; 670; 123-127

44 G. Lopez-Polina, M. Jaafar, F. Guinea, R. Roldan, C. Gomez-Navarro and J. Gomez-Herrero, Carbon, 2017, 124, 42–48.

45 A. Falin, et al., Nat. Commun., 2017, 8, 15815.

46 Q. Peng, W. Ji and S. De, Comput. Mater. Sci., 2012, 56, 11-17.

47 Madsen, G. & Singh, D. Boltztrap. A code for calculating band-structure dependent quantities. Comput. Phys. Commun. 175, 6771, (2006).

48 Y. Fujimoto and S. Saito, Hydrogen adsorption and anomalous electronic properties of nitrogen-doped graphene, Journal of Applied Physics, vol. 115, no. 15, Article ID 153701, 2014

49 H.R. Mahida, Abhishek Patel, Deobrat Singh, Yogesh Sonvane, P. B. Thakor, Rajeev Ahuja First-principles calculations to investigate electronic structure and optical properties of 2D MgCl2 monolayer, Superlattices and Microstructures 162 (2022) 107132

50 H.R. Mahida, D. Singh, Y. Sonvane, S.K. Gupta, P.B. Thakor, MgF2 monolayer as an anti-reflecting material, Solid State Commun. 252 (2017) 22–28, https://doi.org/10.1016/j.ssc.2017.01.005.

51 H.R. Mahida, D. Singh, Y. Sonvane, P. Thakor, R. Ahuja, S. Gupta, The influence of edge structure on the optoelectronic properties of Si2BN quantum dot, J. Appl. Phys. 126 (2019), https://doi.org/10.1063/1.5131149, 0.

52 D. Singh, S.K. Gupta, Y. Sonvane, I. Lukacevic, Antimonene: a monolayer material for ultraviolet optical nanodevices, J. Mater. Chem. C. 4 (2016) 6386–6390,https://doi.org/10.1039/C6TC01913G.

53 D. Singh, V. Shukla, R. Ahuja, Optical excitations and thermoelectric properties of two-dimensional holey graphene, Phys. Rev. B 102 (2020) 75444,https://doi.org/10.1103/PhysRevB.102.075444.

54 A. Khireddine, A. Bouhemadou, S. Alnujaim, N. Guechi, S. Bin-Omran, Y. Al-Douri, R. Khenata, S. Maabed, A.K. Kushwaha, First-principles predictions of the structural, electronic, optical and elastic properties of the zintl-phases AE3GaAs3 (AE= Sr, Ba), Solid State Sci. 114 (2021) 106563

55 S. Hadji, A. Bouhemadou, K. Haddadi, D. Cherrad, R. Khenata, S. Bin-Omran, Y. Al-Douri, Elastic, electronic, optical and thermodynamic properties of Ba3Ca2Si2N6 semiconductor: first-principles predictions, Phys. B Condens. Matter 589 (2020) 412213.

56 Meirzadeh, E., Evans, A.M., Rezaee, M. et. al., A few-layer covalent network of fullerenes. Nature 2023, 613, 71-76.

57 Tromer, R. M.; Ribeiro, L. A.; Galvão, D. S. A DFT study of the electronic, optical, and mechanical properties of a recently synthesized monolayer fullerene network. Chem. Phys. Lett. 2022, 804, 139925.

58 Yu, L.; Xu, J.; Peng, B.; Qin, G.; Su, G.Flat electronic band structure and anisotropic properties of two-dimensional fullerene networks. Submitted on 6 July 2022. arXiv:2207.02781 (accessed 2022-07-30).

59 Yuan, D.; Pi, H.; Jiang, Y.; Zhou, Y. H. L.; Jia, Y.; Su, G.; Fang, Z.; Weng, H.; Ren, X.; Zhang, W. Highly in-plane anisotropic

optical properties of fullerene monolayers. Submitted on 22 July 2022. arXiv:2207.11366 (accessed 2022-07-30)

60 V.K. Yadav, S.H. Mir, J.K. Singh, Density functional theory study of aspirin adsorption on BCN sheets and their hydrogen evolution reaction activity: a comparative study with graphene and hexagonal boron nitride, Chem. Phys. Chem 20 (2019) 1-9.

61 L.A. Ribeiro Junior, M.L. Pereira Junior, W.F. Giozza, R.M. Tromer, Douglas S. Galvao, Thermal Stability and Fracture Patterns of a Recently Synthesized Monolayer Fullerene Network: A Reactive Molecular Dynamics Study Chem. Phys. Lett. 807 (2022), 140075 https://doi.org/10.1016/j.cplett.2022.140075

62 J. H. Los, K. V. Zakharchenko, M. I. Katsnelson, A. Fasolino, Melting temperature of graphene, Physical Review B 91(4) (2015), 045415 https://doi.org/10.1103/PhysRevB.91.045415